Interface-engineered CuS@NiCoSe with lattice strain: Synergizing photothermal conversion, gas adsorption, and stable catalysis for dry reforming of methane

Zhende Li [a], Jianfeng Lu [a], Jing Ding [a], Yukun Hu [b], Weilong Wang [a, *]

[a] School of Materials Science and Engineering, Sun Yat-Sen University, Guangzhou 510006, PR China

[b] Department of Civil, Environmental & Geomatic Engineering, University College London, London WC1E 6BT, United Kingdom

*Corresponding address: School of Materials Science and Engineering, Sun Yat-Sen University, Guangzhou 510006, PR China

*E-mail address: wwlong@mail.sysu.edu.cn;

Abstract

Photothermal synergistic dry reforming of methane (DRM) involves the intricate coupling of photothermal conversion, CH_4/CO_2 adsorption-activation, and complex reaction pathways. The development of a multifunctional integrated catalytic system is thus highly desirable, though achieving efficient synergy among these functions remains a critical challenge. Herein, an interface-engineered hollow CuS@NiCoSe catalyst was synthesized via in situ etching and high-temperature selenization. Strong interfacial interactions induced deliberate lattice strain at the CuS/NiCoSe heterointerface, which orchestrated the synergy between photothermal conversion, enhanced CO_2 adsorption, and stable DRM catalysis. Hollow CuS, characterized by a high specific surface area, promoted gas enrichment and induced lattice strain at the interface through strong interactions with the NiCoSe shell. Such strain modulated

the electronic structure of the active sites, thereby facilitating CH_4/CO_2 activation and C–H bond cleavage. Moreover, the NiCoSe shell enabled efficient photothermal conversion via broad-spectrum solar absorption, providing necessary thermal energy to drive the endothermic DRM.

Introduction

Dry reforming of methane (DRM) is a pivotal carbon-upcycling technology that converts CO_2 and CH_4 into high-value syngas (H_2/CO)[1-4]. Consequently, DRM is regarded as a cornerstone technology for mitigating energy scarcity and addressing climate change. However, conventional thermal DRM requires high operating temperatures (typically >700 °C) to overcome thermodynamic constraints[5-8], leading to substantial energy consumption, severe catalyst deactivation by coking, and metal particle sintering[9-11]. Recent breakthroughs in photothermal catalysis have prompted a paradigm shift: this approach reduces reaction temperatures while enabling the direct participation of photocarriers in catalytic cycles by harnessing the synergy between solar-induced localized heating and photogenerated charge carriers, thereby boosting energy efficiency and reaction activity[12-15]. For industrial feasibility, it is essential not only to integrate three core functionalities—efficient activation of CH_4/CO_2[16], high-capacity gas adsorption[17], and superior photothermal conversion[18]—but also leverage structural design[19] and interface engineering[20] to achieve

synergy among them. Nevertheless, such multifunctional coupling remains a critical and unresolved challenge.

The rapid development of structurally and chemically robust materials, such as ferrites[21-22], perovskites[23-24], metal-organic frameworks (MOFs)[25-26], and transition metal nitrides/selenides[27], has revolutionized photothermal catalysis. Rao et al. engineered Ni-O/Ni-Ni dual sites that converted *CH_3 to *CH_3O at 472 °C, and the Ni–O moiety lowered the *C–O coupling barrier and thereby eliminated filamentous carbon, enabling 230 h of stable operation without observable coking behavior[28]. He et al. reported a Ru single-atom TiO_2-SiO_2 catalyst (Ru-TS), and the resulting Ru–O_v–Ti configuration equalized the adsorption energetics of CH_4 and CO_2 and enforces a barrier-less *C–O recombination pathway, delivering extraordinary syngas production rates (98.52 mmol $gRu^{-1}\cdot h^{-1}$ for CO and 96.50 mmol $gRu^{-1}\cdot h^{-1}$ for H_2) and long-term stability[29]. Moreover, Li et al. designed a flower-like mesoporous TiO_2-Ru-S catalyst in which the mesoporous structure significantly increased the specific surface area of the material, exposed more active sites, and facilitated contact between gases and active sites. The introduction of S effectively prolonged the lifetime of photogenerated carriers and sustained quantitative syngas yield over 100 h of cycling[30]. While these studies highlight the importance of coordination structures[31-32], morphologies[33-34], and defects[35-36], most

efforts focused on optimizing single functionalities, such as active site density or light absorption. Critical gaps remain, particularly regarding the role of the heterointerface and lattice strain in synergizing photothermal conversion, gas adsorption, and catalytic activation, limiting the efficiency of multifunctional integration.

Materials with localized surface plasmon resonance (LSPR) can generate localized electromagnetic fields and thermal energy under illumination, making them promising for photothermal catalysis[37-38]. While noble metals (e.g., Au and Ag) represent classic LSPR materials, their high cost hinders scalable application. In contrast, transition metal selenides exhibit plasmonic-like resonance in the near-infrared region, stemming from Se vacancies that increased the free electron density via collective carrier oscillations, offering a cost-effective alternative. Jyotirmayee Sahu et al. decorated CuS nanosheets with $Zn_{0.5}Cd_{0.5}Se$ quantum dots, achieving efficient photocatalytic H_2O_2 production and p-nitrophenol reduction via LSPR effects[39]. Han et al. constructed a frame-in-cage hybrid (ZnSe–CdSe@NC FC) composed of ZnSe–CdSe embedded within a N-doped carbon matrix, which outperformed single-mode catalysis in CO_2 photoreduction due to synergistic photothermal conversion and abundant active sites[40]. Despite these advances, selenide-based catalysts still lack a deliberate design of heterointerfaces (e.g., core–shell architectures) to induce lattice strain,

which is critical for modulating the electronic structures of active sites and coupling gas adsorption with photothermal conversion.

Herein, a hollow-structured CuS@NiCoSe core–shell photothermal catalyst was established via in situ etching and high-temperature selenization, and lattice strain was induced at the CuS/NiCoSe heterointerface by leveraging interface engineering. The hollow CuS core enhanced gas enrichment owing to its high specific surface area and strong interfacial interactions with the NiCoSe shell, generating lattice strain that modulated the electronic structure of active sites to promote CH_4/CO_2 activation. Moreover, the NiCoSe shell, enriched with Se vacancies, exhibited superior photothermal conversion efficiency via broad-spectrum absorption, accelerating the reaction kinetics under solar irradiation. The evaluation of DRM performance revealed exceptional H_2 and CO production rates (472.5 and 496.3 $mmol \cdot g^{-1} \cdot h^{-1}$, respectively), with unattenuated activity over 100 h of operation. Experimental and theoretical analyses confirmed that the lattice strain mediated synergy between CuS (responsible for gas adsorption and strain induction) and NiCoSe (enabling photothermal conversion and catalytic activation), thereby addressing the critical challenge of multifunctional coupling in photothermal DRM. This work highlights interface engineering and lattice strain as universal strategies for advancing synergistic photothermal catalysis, with broader implications for greenhouse gas

valorization.

2. Experimental section

2.1 Reagents and materials

Cobaltous nitrate hexahydrate (99.99 %, $Co(NO_3)_2·6H_2O$), Nickel nitrate hexahydrate (99.99 %, $Ni(NO_3)_2·6H_2O$), Methanol (99.9 %, MeOH), Sodium sulfide (99%, Na2S), Cupric sulfate (98%, $CuSO_4·5H_2O$), Sodium hydroxide (98%, NaOH), Ascorbic Acid (99%), Sodium sulfate (99%, Na_2SO_4), Sodium thiosulfate (99.5%, Na_2S_2O), Selenium (99.9%), Sodium citrate (98%, $C_6H_5Na_3O_7$), ethyl alcohol (96%, C_2H_5OH) were obtained from Aladin Ltd. (Shanghai, China); 2-Methylimidazole (98 %, 2-MIM) is obtained from Vokai Biotechnology Ltd. (Beijing, China). Unless otherwise stated, all chemicals are of analytical reagent grade and used without further purification.

2.2 Synthesis of CuS

The preparation of CuS was performed as previously reported with appropriate modifications. Sodium hydroxide aqueous solution (20 mL, 4 M) was added to a mixed solution containing $CuSO_4·5H_2O$ (5 mmol), trisodium citrate (1.5 mmol), and deionized water (80 mL). After stirring for 15 minutes, L-ascorbic acid aqueous solution (50 mL, 0.1 M) was added. Following 3 minutes of stirring and 1 hour of aging, the red precipitate of Cu_2O nanocubes (NCs) was collected via multiple centrifugation and washing steps with water and ethanol, and then dried

at 60 ℃ for 12 hours. Subsequently, sodium sulfide aqueous solution (40 mL, 6.25 mM) was added to a suspension of Cu_2O NCs (100 mg) in deionized water (60 mL) for sulfidation over 30 minutes, followed by centrifugation and washing cycles. The obtained Cu_2O@CuS core-shell structure was dispersed in a mixture of deionized water (20 mL) and ethanol (20 mL). The resulting alcoholic suspension was then added to sodium thiosulfate aqueous solution (16 mL, 1.0 M) to etch the Cu_2O core. After 30 minutes, CuS was collected through centrifugation and washing cycles.

2.3 Synthesis of CuS@NiCoSe

CuS (100 mg) was uniformly dispersed in methanol (30 mL), followed by the addition of cobalt nitrate hexahydrate ($Co(NO_3)_2 \cdot 6H_2O$, 50 mg) and nickel nitrate hexahydrate ($Ni(NO_3)_2 \cdot 6H_2O$, 50 mg). The mixture was stirred for 30 minutes to form Solution A. Separately, 2-methylimidazole (0.6 g) was dissolved in methanol (10 mL) to form Solution B. Solution B was rapidly poured into Solution A, and the combined mixture was stirred for 2 hours. The resulting solution was transferred to a Teflon-lined autoclave and subjected to a hydrothermal reaction at 160 °C for 10 hours. The precipitate was collected by centrifugation, washed three times with deionized water, and dried at 50 °C for 10 hours to obtain CuS@NiCo. The as-synthesized CuS@NiCo (100 mg) was mixed with varying amounts of selenium powder (50 mg,

100 mg, and 150 mg). The mixtures were calcined under a nitrogen atmosphere at 500 °C for 3 hours to yield the final CuS@NiCoSe (CNCS) samples. The catalysts were labeled as CNCS-0.5, CNCS, and CNCS-1.5 based on the amount of selenium powder added (0.5, 1.0, and 1.5 equivalents relative to CuS@NiCo, respectively). Throughout the manuscript, all instances of "CNCS" without a numerical suffix denote "CNCS-1.0".

2.4 Instruments

The scanning electron microscopy (SEM) analysis was performed using a Japan-Hitachi-Regulus 8230 scanning electron microscope. The morphology was characterized by transmission electron microscopy (TEM, JEOL F200) and high-resolution transmission electron microscopy (HRTEM, JEOL F200). Energy dispersive X-ray spectroscopy (EDS) was carried out using 4 in-column Super-X detectors. The powder X-ray diffraction (XRD) characterizations of all samples were carried out on a Rigaku D/ MAX 2550 diffract meter (Cu K radiation, λ = 1.5406 Å) operating at 40 KV and 40 mA, data was collected in the range of 10-80◦ (2 theta). The Raman tests were conducted on Renishaw's in Via Raman with 532 nm laser as the excitation light source. The ultraviolet-visible (UV–vis) absorption spectra were acquired for the dry-pressed disk samples using a Scan UV–vis spectrophotometer (UV-3600 plus) equipped with an integrating sphere assembly, using $BaSO_4$ as the

reflectance sample. X-ray photoelectron spectroscopy (XPS) was performed on a ThermoFisher Nexsa system with Al Kα radiation operated at 250 W. Electron paramagnetic resonance (EPR) was carried out on a Bruker - EMXPlus-10/12 instrument. CO_2 temperature programmed desorption (CO_2-TPD) was carried out on Tianjin-TP5080. A thermogravimetric analyzer (TGA, PE-TGA4000) was used to characterize the carbon deposits of the spent catalyst. The Time-resolved photoluminescence (TRPL) spectra were carried out by a FLS 1000 spectrometer with a 360 nm LED laser as the light source.

2.5 In Situ Experiments.

In situ diffuse reflectance infrared Fourier transform spectroscopy (In situ DRIFTS) was recorded by a Bruker Invenio S infrared spectrometer equipped with a liquid nitrogen-cooled mercury-cadmium-telluride (MCT) detector. The prepared samples were firstly degassed at 70 °C for 2 h under flow of Ar (50 ml min^{-1}), and cooled to room temperature under flow of Ar (50 ml min^{-1}). Then, the catalysts sealed in the chamber for introducing the flowed mixture gas (CH_4: CO_2=1:1), samples were collected respectively at 100℃, 300℃ and 500℃ under dark. Subsequently, under the irradiation of a 300 W xenon lamp, intermediate signals were acquired at 10-minute intervals, with a total of 5 acquisitions performed.

In situ X-ray Photoelectron Spectroscopy (In situ XPS) was obtained on a Thermo SCIENTIFIC ESCALAB 250Xi spectrometer. This spectrometer was equipped with a window that could control the passage of light (monochromatic Al Ka of X-ray photoelectron spectroscopy, with hv = 1486.6 eV), had a power of 150 W and a beam spot of 500 μm. The fixed transmission energy of the energy analyzer was 30 eV. The specific testing process was as follows: Firstly, the spectra of the target samples were scanned under dark conditions. Then, after being placed in a darkroom for 300 minutes, the samples were irradiated with a 300 W xenon lamp, and the spectra were scanned after the lamp was turned on. Finally, the overall spectra of various elements and the corresponding atomic orbital spectra were obtained.

2.6 Electromagnetic Measurements

The electrochemical measurements were measured on an electrochemical analyzer (Zahner, Zennium) at room temperature. The standard three-electrode system was composed of a working electrode, a graphite carbon rod as the counter electrode, and a saturated calomel electrode as the reference electrode. The working electrode was prepared by a fluorine-doped tin oxide (FTO) deposited with a sample film. Typically, 5 mg photocatalysts were dispersed in 0.5 mL ethanol, then 0.02 mL of the solution was dip-coated on the FTO surface and dried under atmospheric conditions at room temperature to form film. The area

of formed film was fixed at 1 cm2. The transient photocurrent responses of different samples were carried out in N_2 saturated 0.5 M Na_2SO_4 aqueous solution under 300 W Xe lamp irradiation. The data of electrochemical impedance spectroscopy (EIS) were obtained in the frequency range from 100 kHz to 0.1 Hz under amplitude of 10 mV using N_2 saturated potassium ferricyanide mixed electrolyte without Xe lamp irradiation.

2.7 Density functional theory (DFT) calculation

The Vienna Ab-initio Simulation Package (VASP) was employed to conduct all Density Functional Theory (DFT) calculations. The Perdew-Burke-Ernzerhof (PBE) exchange-correlation functional, employing the generalized gradient approximation (GGA) method with Grimme D3 dispersion correction, was utilized in this study. The projected augmented wave (PAW) method was utilized to describe core-valence interactions in all DFT calculations. The energy cutoff for plane wave expansions was set to 550 eV, and the $1 \times 1 \times 1$ Monkhorst-Pack grid k-points were used to sample the Brillouin zone integration for structural optimization of surface structures. Structural optimization was carried out with energy and force convergence criteria setting at 1.0×10-5 eV and 0.02 eV Å-1, respectively.

2.8 Catalytic tests

The methane dry reforming reaction performance was evaluated in

an atmospheric pressure micro-photothermal reactor (BEIJING CHINA EDUCATION AU-LIGHT CO., LTD GEL-GPPCM). Fig. S1a-e shows the schematic diagram of the microphotothermal reactor. The catalyst was placed in a round quartz tube 49.5 cm long with an inner diameter of 6 mm and an outer diameter of 10 mm, the ends of which were filled with an appropriate amount of quartz wool, and the temperature of the reaction was detected by a K-type thermocouple placed underneath the catalyst. A 300W xenon lamp (BEIJING CHINA EDUCATION AU-LIGHT CO., LTD CEL-HXF300-T3) was used as the light source (Fig. S1c) to irradiate from the catalyst side through the quartz window. Typically, 50 mg of catalyst was placed in the appropriate position in a quartz tube and reheated under a 20 mL $\cdot$ min^{-1} H_2 atmosphere for reduction to 500 ℃ for 2 h before being subjected to thermal and photothermal catalytic reactions. Then, the heating was stopped, and H_2 was replaced by N_2 until the temperature was reduced to 150 ℃. Finally, a mixture of 20% CH_4, 20% CO_2, and 60% N_2 was introduced with a flow rate of 50 mL • min^{-1}. After stabilisation for 30 min, the products were collected under light and dark conditions, respectively. The above procedure was repeated at 500 °C, 550 °C, 600 °C and 650 °C (The temperature is the same before and after the light). Collected gases were analysed by gas chromatography and the production rates of H_2 and CO as well as the ratio of H_2 to CO were calculated using Equations (Eqs.) 1 and 2:

$$Y_{H_2} = \frac{n_{H_2}}{2n_{CH_4,in} - 2n_{CH_4,out}} \quad \text{Eq.1}$$

$$Y_{CO} = \frac{n_{CO}}{(n_{CH_4,in} + n_{CO_2,in}) - (n_{CH_4,out} + n_{CO_2,out})} \quad \text{Eq.2}$$

Y_{H2} and Y_{CO} represent the production rates of H_2 and CO, respectively. Here, $n_{CH4,in}$ and $n_{CO2,in}$ denote the molar amounts of CH_4 and CO_2 introduced into the system, while $n_{CH4,out}$, $n_{CO2,out}$, $n_{H2,out}$ and $n_{CO2,out}$ indicate the molar amounts of CH_4, CO_2, H_2 and CO flowing out of the system, respectively.

2.9 CO_2-TPD Experiment

The CO_2-temperature programmed desorption (CO_2-TPD) tests were performed using a BELCata II instrument (MicrotracBEL, Japan). The detailed testing procedure was as follows: Approximately 50 mg of the sample was weighed and placed in a quartz reaction tube. First, the sample was subjected to a drying pretreatment by heating from room temperature to 300 °C at a rate of 10 °C/min, with high-purity He gas purging at a flow rate of 50 mL/min for 1 h. After pretreatment, the sample was cooled to 50 °C, and a 10 vol% CO_2/He mixed gas was introduced into the system until adsorption saturation was achieved. Subsequently, the gas was switched back to high-purity He (maintained at 50 mL/min) for a 1 h purge to remove physically adsorbed CO_2 from the sample surface. Finally, the sample was heated to 650 °C at a heating rate of 10 °C/min under a continuous He flow (50 mL/min), and the desorbed

gas was detected in real time using a thermal conductivity detector (TCD).

2.10 Photothermal conversion performance Test.

The photothermal conversion test was performed using an 808 nm laser beam (MDL-H-808) as the light source. A glass slide with a centrally fabricated circular well (6 mm diameter) served as the sample platform, positioned such that the laser beam formed a ~10 mm diameter spot on the platform. A thermocouple probe was secured within the well, and the powdered sample was uniformly packed into the circular recess to fully cover the probe tip. After compacting the sample, the temperature response under varying laser power densities was monitored via the thermocouple.

3. Results and discussion

A hollow core-shell CuS@NiCoSe-1.0 (CNCS) catalyst was fabricated via template etching combined with in-situ growth (synthesis scheme: Fig. 1a; detailed procedures in Experimental Section). Its structural and phase properties were verified by comprehensive characterization. Cubic Cu_2O was first synthesized as the CuS precursor. X-ray diffraction (XRD) analysis (Fig. S2a) exhibited sharp, symmetric diffraction peaks at 2θ = 29.3°, 36.2°, 42.2°, 61.4°, 73.5°, and 77.5°, which are strictly indexed to the (110), (111), (200), (220), (311), and (222) planes of cubic Cu_2O (JCPDS 05-0667), confirming the formation

of high-purity Cu_2O. Scanning electron microscopy (SEM) and transmission electron microscopy (TEM) images (Fig. S2b and S3) revealed well-defined hexahedral particles (1.2 μm in diameter) with smooth surfaces, distinct edges, and uniform contrast, characteristic of a dense solid structure. Geometric phase analysis (GPA) of inverse Fourier-transformed HRTEM images (Fig. S4) revealed negligible lattice strain. Subsequent sulfidation and in-situ etching converted Cu_2O to hollow CuS. XRD patterns (Fig. S5) displayed characteristic peaks at $2\theta \approx 29.5°$, 31.8°, 32.9°, 47.9°, and 52.7°, corresponding to the (102), (103), (006), (110), and (108) planes of hexagonal CuS (JCPDS 06-0464), verifying phase-pure CuS. SEM (Fig. S6) confirmed retention of the polyhedral morphology with increased surface roughness; fractured regions exposed internal cavities (shell thickness: 50–70 nm, cavity fraction > 80%). TEM further validated the hollow architecture (Fig. S7), with GPA analysis (no significant contrast variation) confirming absent lattice strain (Fig. S8). After conformal coating of NiCoSe on CuS, XRD patterns (Fig. S9a) matched NiCoSe (JCPDS 88-1711), confirming successful selenide integration. SEM revealed vertically oriented NiCoSe nanosheets decorating the CuS surface (as shown in Fig. 1b); fractured regions exposed the hollow core and layered shell, confirming the core-shell configuration. Elemental mapping confirmed homogeneous distribution of Cu, S, Ni, Co, and Se (Fig. 1h). TEM images (Fig. 1c and

d) exhibited "dark-bright-dark" edge contrast (CuS shell → cavity → NiCoSe layer), indicative of an intact heterostructure. High-resolution TEM (Fig. 1e) identified lattice fringes corresponding to NiCoSe (210) planes. Critical to performance, GPA (Fig. S9d) analysis showed pronounced contrast variation—distinct from Cu_2O and CuS—indicating significant lattice strain induced by NiCoSe. This strain, arising from CuS/NiCoSe lattice mismatch, induces a downshift in Cu 2p binding energy (Fig. 1f). Meanwhile, the electron enrichment of Cu also renders Ni sites electron-enriched via interfacial charge transfer (Fig. S10b). This synergistic electronic effect enhances the polarization of C-H bonds in CH_4, facilitating the dissociation process: Cu promotes bond pre-activation through polar interactions, while Ni, as the primary active center, completes the dissociation process. Additionally, strain-induced lattice distortion elevates Se vacancy concentrations (Fig. 1g). These vacancies, via coordinatively unsaturated Ni^{2+}/Co^{3+} sites, strengthen CO_2 adsorption (CO_2 → CO_2*) and boost uptake. Enhanced electron localization at defects further lowers CO_2 activation barriers, synergistically promoting catalytic activity.

X-ray photoelectron spectroscopy (XPS) analysis probed the elemental valence states and interfacial electronic interactions in CuS and CuS@NiCoSe (Fig. 1f). In pristine CuS, Cu 2p core-level peaks appear at 952.07 eV (Cu $2p_{1/2}$) and 932.12 eV (Cu $2p_{3/2}$), whereas those in CNCS

exhibit a subtle downshift to lower binding energies. This shift originates from dual effects: electron transfer across the NiCoSe-CuS interface and lattice strain at the heterointerface. Specifically, strain modulates Cu's binding energy by altering atomic spacing and electron cloud distribution, directly inducing the observed XPS peak displacement. The S 2p XPS spectra (Fig. S10a) display analogous behavior: heterojunction formation between CuS and NiCoSe triggers interfacial band bending, shifting the Fermi level (E_F) of S atoms to reduce ionization energy. Concurrently, lattice strain at the interface perturbs S's electronic orbital hybridization, enhancing electron delocalization and weakening nuclear-electron binding. These synergistic effects collectively drive the downshift of S characteristic peaks. Electron paramagnetic resonance (EPR) spectroscopy validated Se vacancies, with the signature signal at g = 2.003 (Fig. 1g) serving as a definitive marker. Notably, this signal's intensity first increases then decreases with rising Se content—evidence that excess Se preferentially occupies intrinsic vacancy sites in the NiCoSe lattice, thereby reducing Se vacancy concentration (Fig. S11 and S12).

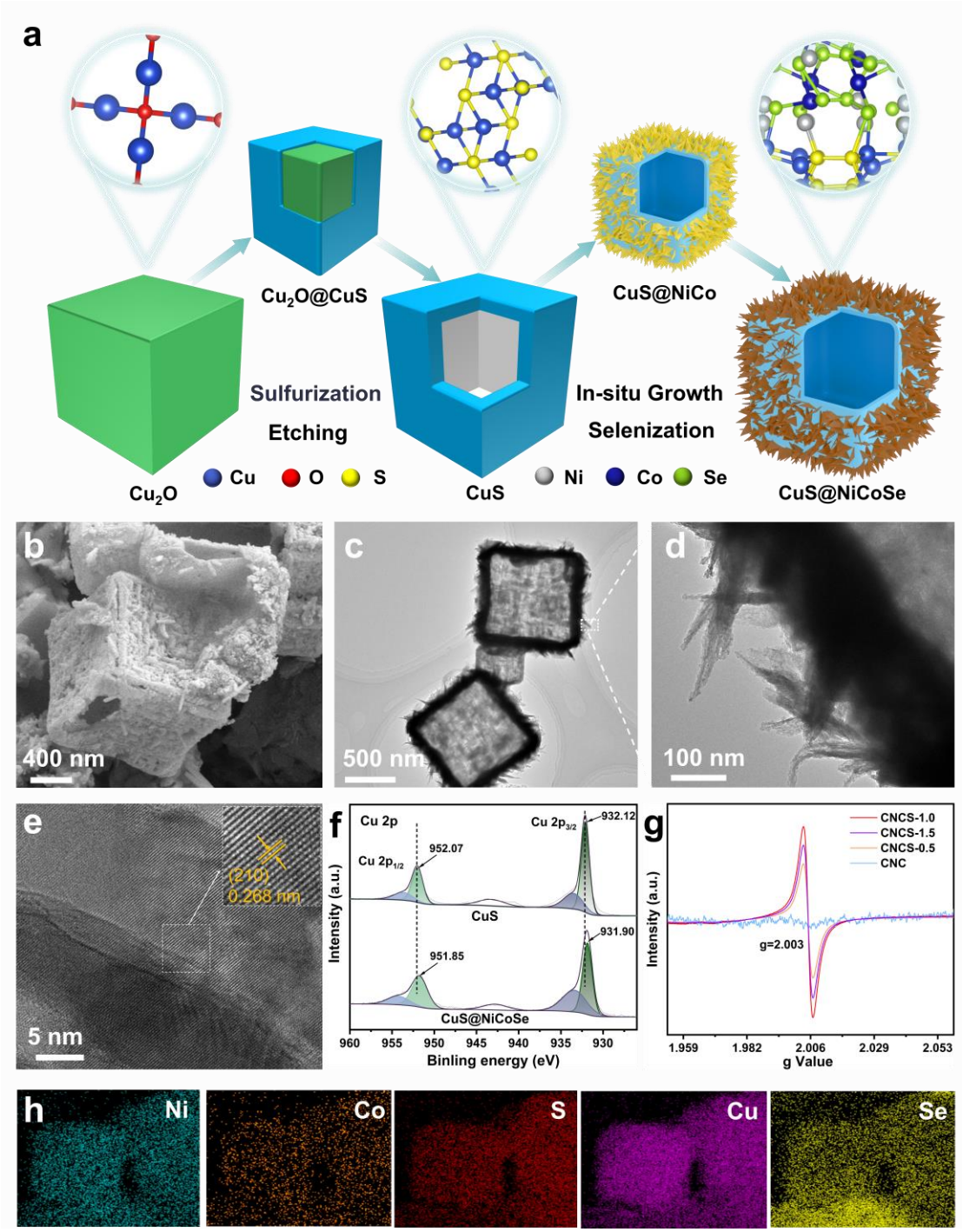

Fig. 1. (a) The fabrication process of CNCS. (b) SEM image of CNCS. (c) and (d) TEM images of CNCS. (e) HRTEM image of CNCS. (f) XPS spectra of CNCS. (g) EPR spectra of different catalysts. (h) EDS elements mapping images of CNCS.

A photothermal micro-flow reactor (equipped with a 300 W xenon lamp as the light source) was utilized to systematically investigate the effects of catalyst type (as shown in Fig.S1), reaction temperature, illumination conditions, and syngas ratio on the performance of

CuS@NiCoSe (CNCS) in photothermally driven dry reforming of methane (DRM). Special emphasis was placed on deciphering how Se concentration modulates catalytic activity. Experimental results reveal that under photothermal conditions (as shown in Fig. 2a and Fig. S13), the conversions of CH_4 and CO_2 over all catalyst variants increase with temperature elevation—consistent with the thermodynamic limitations of DRM—yet distinct discrepancies in catalytic activity remain. CuS exhibits negligible conversion efficiency within 500–650 °C, primarily due to insufficient active sites. The non-selenized CuS@NiCo (CNC) catalyst achieves CH_4 and CO_2 conversions of 64.7% and 68.3% at 650 °C, respectively, which are 1.55- and 1.54-fold higher than those at 500 °C, but still fall short of industrial requirements. In contrast, selenization significantly enhances the performance of CNC, with catalytic activity showing a non-linear dependence on Se dosage: at 650 °C, CH_4 conversion initially increases from 81.7% to 87.7% with increasing Se content, followed by a decrease to 83.2%. This behavior arises from Se-mediated regulation of catalyst defect structures and photogenerated carrier dynamics: at low Se concentrations, moderate Se vacancies enhance CO_2 adsorption and CH_4 dissociation via coordinatively unsaturated Ni/Co sites, lowering activation barriers for C-H and C=O bonds while acting as efficient electron traps to suppress carrier recombination; excess Se, however, occupies lattice vacancies to

reduce active sites and serves as strong electron-hole recombination centers, shortening carrier lifetimes and ultimately degrading catalytic activity. To highlight the contribution of Ni in DRM, we tested the CH_4 conversion of CuS@Ni and CuS@Co under photothermal conditions at 650 °C and calculated the H_2/CO ratio. The results show that (as presented in Fig. S14), compared with CuS (which exhibited a CH_4 conversion of 14.1%), CuS@Ni displayed significantly enhanced dry reforming activity, achieving a CH_4 conversion of 52.2%. This conversion was also higher than that of CuS@Co (which showed a CH_4 conversion of 41.3%), and the H_2/CO ratio remained stable at 0.78. This remarkable performance enhancement directly confirms the unique role of Ni in the dry reforming reaction. Furthermore, by comparing CuS@Ni with CNC and CNCS, we can further verify the synergistic promotional effect of Co, while emphasizing the irreplaceability of Ni as the main active component.

A direct comparison of H_2 production under photothermal versus purely thermal conditions quantifies the performance boost induced by light irradiation. As evident in Fig. 2b, illumination enhances DRM activity to varying extents, with CNCS-1.0 achieving a H_2 production rate of 472.5 mmol g^{-1} h^{-1} under photothermal conditions. Notably, CNCS-1.0 exhibits the most substantial improvement (35.2%) relative to thermal-only conditions, arising from the efficient coupling of its selenide

structure with photothermal synergistic mechanisms. In CuS@NiCoSe, the NiCoSe bimetallic selenide component enables broadband light absorption spanning ultraviolet-visible-near-infrared regions (Figure S15)—far broader than that of CuS@NiCo or CuS—due to its tailored band structure and Se-vacancy-induced plasmonic-like resonance (strong near-infrared absorption). This enhanced light-harvesting capability allows CuS@NiCoSe to reach higher surface temperatures under identical illumination while directly lowering reaction activation barriers via photoexcitation (light-assisted thermal catalysis). In contrast, CNC and CuS exhibit weaker photothermal conversion and barrier reduction effects, stemming from their limited absorption spectra. The CNCS catalyst exhibits superior catalytic performance at different temperatures compared with the state-of-the-art works in the field (Fig. 3c).

The H_2/CO ratio and its stability are pivotal to catalyst design, mechanistic elucidation, and the industrialization of dry reforming of methane (DRM). Having established the performance advantages of CNCS, the H_2/CO ratios under photothermal versus pure thermal conditions were determined over the 500–650°C range. CNCS consistently exhibited higher ratios under photothermal conditions, highlighting light's efficacy in suppressing side reactions (Fig, S15). Photoexcited holes preferentially accumulate near Se vacancies, participating predominantly in CO_2* activation (CO_2* → CO* + O*)

rather than reacting with H_2 to initiate the reverse water-gas shift (RWGS) reaction. This selectivity reduces the probability of H_2-CO_2 interactions, thereby minimizing H_2 consumption. Notably, CNCS outperforms previously reported catalysts across the temperature range, as benchmarked against literature data.

Catalytic stability represents a paramount metric for industrial DRM applications. Remarkably, the CNCS catalyst demonstrates exceptional long-term stability with negligible deactivation: after 100 h of photothermal testing, the H_2 production rate remains at 451.2 mmol g^{-1} h^{-1} while maintaining a stable syngas ratio (Fig. 3d). In contrast, stability diverges markedly between photothermal and pure thermal conditions: after 50 h, the H_2 production rate under pure thermal conditions plummets to 58.6% of its initial value, with the H_2/CO ratio decreasing from 0.95 (photothermal) to 0.68. Coke formation represents the dominant deactivation pathway in DRM. Under photothermal conditions, photogenerated holes react preferentially with carbonaceous intermediates, synergizing with CO_2-mediated oxidation ($C^* + CO_2 \rightarrow 2CO$) to establish a photo-assisted decoking mechanism that markedly reduces coking rates. Conversely, pure thermal conditions rely exclusively on CO_2-driven thermal oxidation, which exhibits low decoking efficiency and leads to coke buildup that masks active sites. Post-reaction coking behavior was characterized using transmission

electron microscopy (TEM) and thermogravimetric analysis (TGA). Striking differences in catalyst surface states emerged after 100 h of reaction under the two conditions: TEM images (Fig. S17) reveal no appreciable amorphous carbon deposits on the photothermally treated catalyst, with its hollow structure remaining intact; whereas the thermally treated counterpart is encased in a thick amorphous carbon layer. TGA analysis (Fig. S18a) corroborates these observations: the mass loss rate (arising primarily from high-temperature coke decomposition) reaches 10.6 % for the thermally treated catalyst, far exceeding the 1.7 % observed for the photothermally treated sample. Furthermore, the I_G/I_D ratio in Raman spectroscopy is commonly used to evaluate the degree of graphitization. The higher the degree of graphitization, the more difficult it is to eliminate carbon deposition. The I_G/I_D value (Fig. S18b) after the photothermal reaction (1.12) is much lower than that after the thermal-only reaction (1.65), indicating that the catalyst exhibits superior carbon deposition resistance under photothermal conditions. These findings collectively demonstrate that photothermal synergy not only enhances DRM catalytic efficiency but also markedly improves catalytic stability by mitigating coke formation.

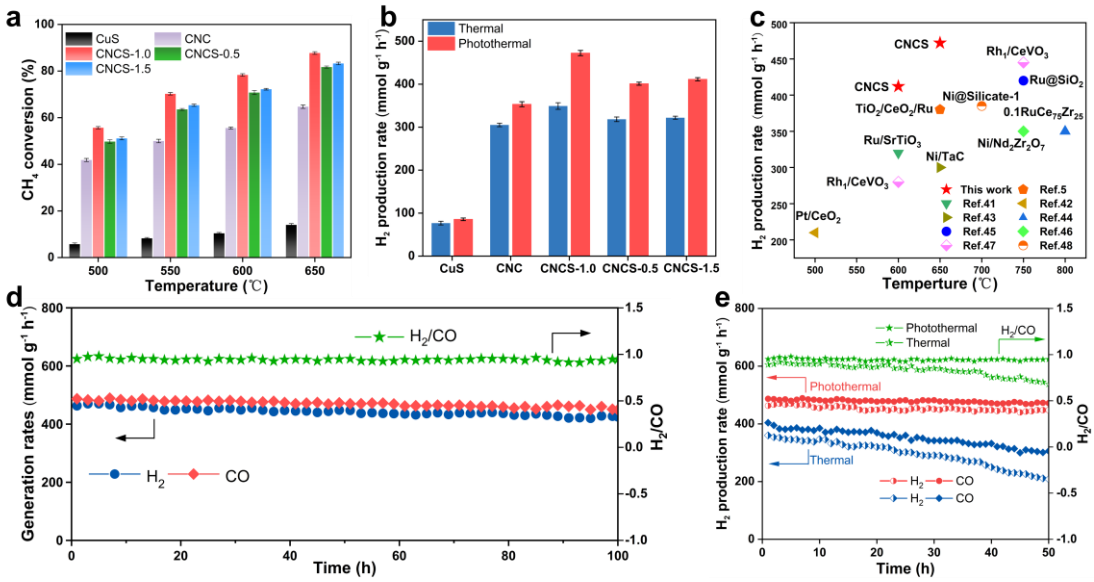

Fig. 2. (a) Conversion rate of CH_4 for different catalysts is affected by temperature. (b) The H_2 generation rates of different catalysts under photothermal/thermal conditions. (c) Comparisons of yields of H_2 of CNCS with the results in literatures. (d) The catalytic stability of H_2 and CO generation rates over 100 h. (e) The catalytic stability of H_2 and CO generation rates over 50 h under photothermal/thermal conditions. All error bars come from the average of at least three in-dependent tests.

To unravel the synergistic regulatory mechanism of temperature and light on reaction pathways, in situ diffuse reflectance infrared Fourier transform spectroscopy (In situ DRIFTS) was employed to track the dynamic evolution of surface intermediates during photothermal DRM. In situ DRIFTS tests exposed the catalyst to a CH_4/CO_2 mixture under gradually increasing temperature and light irradiation (see **2.5 In Situ Experiments** for details). Results showed that CH_4 (3016 cm^{-1}) and CO_2 (2349 cm^{-1}) characteristic peak intensities increased under both thermal-only and photothermal conditions (as shown in Fig. S19 and Fig.3a). Enhanced intensities indicate stronger adsorption and activation of CH_4/CO_2 on active sites, as temperature supplies thermal energy to overcome adsorption barriers and light enhances charge transfer to

strengthen CH_4/CO_2-catalyst interactions—confirming the light-heat synergy in promoting reactant activation. Additionally, the characteristic peak of gaseous CO at 2174 cm^{-1} fluctuates significantly under illumination (Fig. 3b)—a phenomenon that demonstrates light rapidly accelerates CO generation. This is attributed to light irradiation accelerating the conversion of *CHO/*COOH to CO via photoexcited charges. The dynamic variation of this peak is consistent with the evolution of *CHO and *COOH intermediates, confirming an efficient CO formation pathway under photothermal conditions.

Notably, light exerted a more pronounced effect on CO_2 activation: as shown in Fig. 3c, the characteristic peaks of asymmetric *OCO intermediates (vas(OCO)) at 1547 cm^{-1} and 1512 cm^{-1} exhibited intensified fluctuations under illumination. *OCO is a key intermediate in CO_2 activation; light promoted *OCO formation, indicating its facilitation of CO_2 activation. The *CH_xOCO species at 1425 cm^{-1} directly reflects the coupling product of *OCO and CH_x—one of the rate-limiting steps in DRM. Light irradiation accelerated the coupling rate of *CH_xOCO, thereby enhancing the DRM reaction rate. Under light irradiation, a new vibrational band at 1725 cm^{-1}, assigned to *CHO intermediates, indicated that CH_x species from CH_4 dissociation combine with O atoms derived from CO_2 dissociation to form *CHO. This reaction step effectively inhibits the dissociation of the last hydrogen atom from CH_4 (which

would form carbon deposition), holding significant practical importance for the catalytic stability of the catalyst. Additionally, a new band at 1649 cm^{-1}, attributed to the characteristic vibration of *COOH, further revealed the coupling pathway between CO_2 and hydrogen-containing intermediates.

The dynamic evolution of hydroxyl species is critical for decoding the reaction intermediate network (Fig. 3d). Two types of hydroxyl groups were identified in the 3500-3800 cm^{-1} range: terminal hydroxyls (Type I) and bridging hydroxyls (Type II). Type I hydroxyls are associated with *COOH intermediates, while Type II hydroxyls correspond to H_2O generated via the reverse water-gas shift (RWGS) reaction ($CO_2 + H_2 \rightarrow CO + H_2O$). The RWGS reaction initiates at 500°C; upon initial light exposure, the intensity of hydroxyl peaks increases (promoting RWGS), whereas it weakens after light stabilizes (inhibiting RWGS), indicating that light exerts a dynamic regulatory effect on RWGS. In situ DRIFTS confirms the presence of a richer pool of intermediates (e.g., *CH_xOCO, *CHO, *COOH) during photothermal DRM, alongside enhanced signals of *OCO and CO. These observations demonstrate that light strengthens the main reaction pathway by promoting the activation and coupling of CH_4 and CO_2, as well as regulating the RWGS side reaction—providing direct intermediate-level evidence for the photothermal synergistic enhancement of DRM

efficiency.

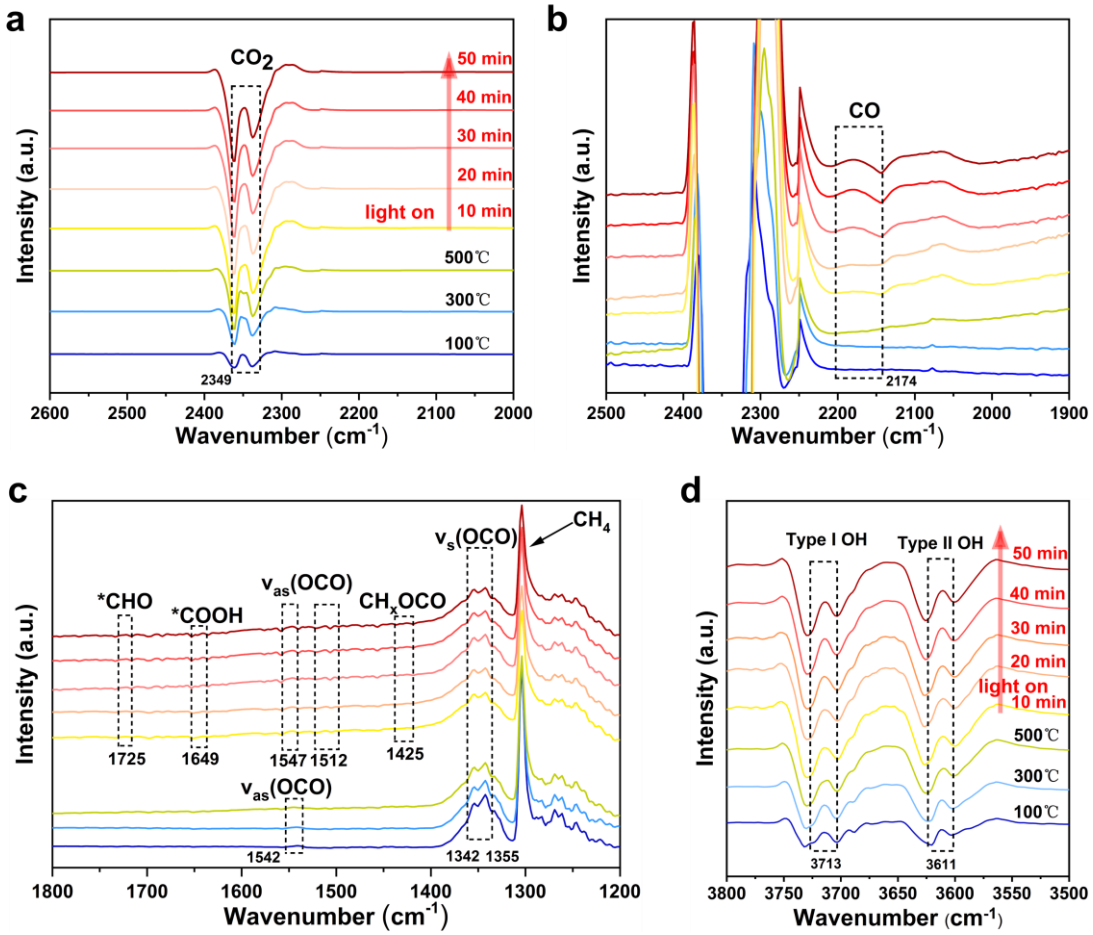

Fig. 3. In situ DRIFT analysis of DRM mechanism on CNCS: (a) 2000-2600 cm^{-1}. (b)1900-2500 cm^{-1}. (c)1200-1800cm^{-1}. (d) 3500–3800 cm^{-1} spectra under photothermal and thermal conditions.

To decipher the photo-driven mechanism and core performance metrics of CNCS in photothermal dry reforming of methane (DRM), we employed in situ characterizations and performance evaluations to systematically interrogate its photogenerated carrier dynamics, CO_2 adsorption behavior, and photothermal conversion efficiency. In situ X-ray photoelectron spectroscopy (In suit XPS) unveiled the charge transfer pathway under illumination: upon photoexcitation, the Cu $2p_{3/2}$ and Cu $2p_{1/2}$ peaks exhibited negative shifts of 0.14 eV and 0.23 eV,

respectively, indicative of photogenerated holes migrating toward the CuS surface. Conversely, the Ni, Co, and Se peaks displayed positive shifts, confirming electron transfer to the NiCoSe component (Fig. 4a–4c and S20). This phenomenon arises from the built-in electric field established at the CuS/NiCoSe interface due to Fermi level disparities (oriented from NiCoSe to CuS), which facilitates directional charge migration—electrons to NiCoSe and holes to CuS—thereby accelerating charge separation. Photocurrent measurements corroborated this mechanism, revealing a 2.5-fold enhancement in photocurrent density for CNCS relative to CuS (Fig. 4d), underscoring the role of NiCoSe in promoting interfacial charge separation. Photoluminescence (PL) spectroscopy (Fig. 4e) revealed that under 261 nm UV excitation, all samples emitted at 420 nm via radiative recombination, yet CNCS exhibited a markedly diminished PL intensity compared to CuS and non-selenized CNC. This attenuation reflects reduced carrier recombination, attributed to the energy level gradient between the CuS core and NiCoSe shell, which spatially separates electron–hole pairs. In contrast, CuS@NiCo exhibited elevated recombination rates due to limited active sites. Time-resolved photoluminescence (TRPL) measurements (Fig. 4f) further confirmed that NiCoSe incorporation extended the carrier lifetime from 1.52 to 2.71 ns, providing prolonged charge availability for photochemical reactions.

The CO_2 adsorption capacity is a critical determinant of DRM efficiency. Owing to safety constraints associated with high-temperature methane adsorption measurements, the present study focused on quantifying CO_2 uptake at 650 °C (DRM operating temperature, Fig. 4g). The CO_2 temperature programmed desorption (CO_2-TPD) results show that CNCS exhibits a significantly enhanced CO_2 adsorption capacity, which is 3.38 times higher than that of NiCoSe (without CuS). Additionally, the CO_2 adsorption capacity of CNCS exhibits an obvious trend of first increasing and then decreasing with the variation of Se content. This phenomenon arises from Se-mediated modulation: an optimal Se concentration enables p-d orbital hybridization between Se (p-orbital) and Ni/Co (d-orbital), which diminishes the localization of Co 3d states and elevates the electron density near the Fermi level, thereby reinforcing CO_2 adsorption and activation. Conversely, excess Se leads to over-encapsulation of NiCo active sites, impairing their capacity for CO_2 adsorption.

Photothermal conversion efficiency serves as a cornerstone for photothermal-synergistic DRM. Its performance was characterized via light-induced temperature evolution and simulated sunlight tests: under illumination without external heating, CNCS exhibits a rapid temperature rise with stable heat dissipation, and attains equilibrium swiftly upon light termination, indicative of an efficient photothermal response (Fig. 4h).

Infrared imaging under simulated sunlight (Fig. 4i) further corroborates that the central temperature of CNCS (72.8 °C) is significantly higher than that of CuS (50.6 °C), demonstrating that the incorporation of NiCoSe enhances photothermal conversion efficiency. The underlying mechanism is associated with interfacial electronic structure modulation (Fig. 4j): due to disparities in work function and Fermi level, CuS and NiCoSe undergo energy level reconstruction, with upward band bending on the NiCoSe side and downward band bending on the CuS side, resulting in the formation of a Schottky barrier. This barrier not only accelerates the directional transfer of electrons from CuS to NiCoSe but also suppresses electron backflow, thereby promoting the separation of photogenerated electron-hole pairs and synergistically enhancing both photothermal conversion and charge utilization efficiency.

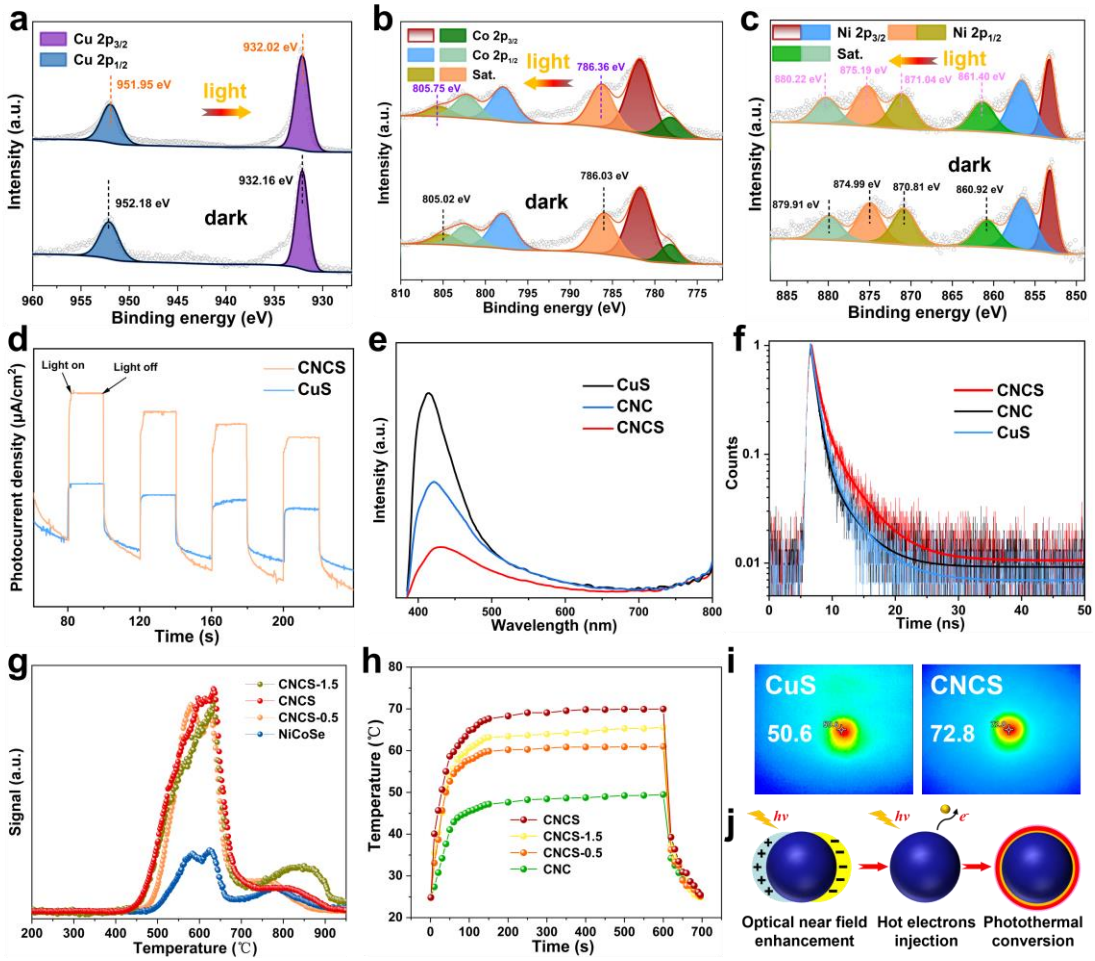

Fig. 4. In situ XPS spectra of (a) Cu 2p, (b) Co 2p, (c) Ni 2p of CNCS under photothermal and thermal conditions. (d) Transient photocurrent response of CNCS and CuS. (e) Photoluminescence spectra of different catalysts. (f) Time-resolved photoluminescence spectra of different catalysts. (g) CO_2-TPD spectra of different catalysts. (h) The time-dependent temperature curves for prepared samples under the light intensity of 0.6 W cm^{-2}. (i) Infrared images of the catalyst under one sun irradiation. (j) Schematic diagram illustrating of LSPR effect of CNCS.

Density functional theory (DFT) calculations systematically unravel the adsorption behaviors of CH_4 and CO_2, reaction pathways, and evolution of key intermediates during CNCS-catalyzed dry reforming of methane (DRM), providing atomic-scale theoretical insights into the experimental observations. First, the adsorption energies of CO_2 on CNCS and NCS were calculated (as shown in Fig. S23). CNCS exhibited a more negative adsorption energy for CO_2, indicating that the CuS

component adsorbed more CO_2 owing to its larger specific surface area and more adsorption sites. This result is consistent with the CO_2-TPD test results (Fig. 4g). Additionally, two distinct adsorption configurations of CH_4 and CO_2 on the CNCS surface—horizontal and vertical configurations—were calculated (Figs. 5a and 5b), which exert a significant impact on the progression of subsequent reactions. After structural optimization (Fig. S21 and 22), significant differences in adsorption energy and reaction activity were calculated. For CH_4, horizontal adsorption exhibits a slightly lower adsorption energy (-0.44 eV) compared to vertical adsorption (-0.40 eV, more thermodynamically stable). However, horizontal adsorption facilitates homolytic dissociation of CH_4 with a substantially reduced energy barrier, leading to excessively rapid CH_4 dissociation that surpasses the carbon elimination capacity of CO_2 ($CO_2 + C^* \rightarrow 2CO$). This imbalance readily triggers the Boudouard reaction ($2CO \rightarrow C^* + CO_2$), resulting in coke deposition. In contrast, vertical adsorption of CO_2 positions its C atom in closer proximity to NiCo active sites, enabling more efficient electron acceptance for activation into intermediates such as OCO*. This promotes coupling with H* species derived from CH_4 dissociation (e.g., $OCO^* + H^* \rightarrow COOH^*$), accelerating the formation of CO and H_2 and thus yielding superior catalytic activity.

Comparative reaction pathway calculations between CNCS and CuS

(Fig. 5d) highlight CNCS's distinct advantages in key DRM steps. CNCS exhibits lower adsorption free energies for CH_4 and CO_2 than CuS, indicating stronger affinity of NiCo active sites toward reactants—facilitating reaction initiation. The dissociation of CH_4* to CH_3* and H*, a rate-determining step in DRM, shows a substantially lower energy barrier on CNCS (0.39 eV) versus CuS (0.91 eV). This arises from electronic interplay between Ni, Co, and Cu, which redistributes electron density at active sites, weakening C-H bonds, lowering dissociation barriers, and markedly enhancing reaction kinetics. Coke formation in DRM primarily originates from CH_4 deep cracking ($CH^* \rightarrow C^* + H^*$) or CO_2 disproportionation, with CH_4 cracking dominating at high temperatures. DFT calculations (Fig. 5c) reveal striking selectivity in CH* evolution on CNCS: CH* preferentially couples with O* from CO_2 dissociation to form CHO* (with lower reaction barriers) rather than directly cracking into C*. This is in full agreement with experimental TG and TEM results showing "significantly reduced coke deposition on CNCS under photothermal conditions," confirming that CHO* formation redirects CH_4 cracking pathways to inherently suppress coke genesis.

Integrating DFT calculations and experimental data, the "adsorption-photothermal-activation" synergistic mechanism for CNCS-catalyzed DRM is proposed (Fig. 5e). CNCS's hollow structure

provides abundant adsorption sites for CH_4 and CO_2, boosting reactant concentrations. Under illumination, CNCS converts light energy to heat to accelerate DRM thermodynamics; concurrently, photogenerated carriers modulate electron transfer via NiCo sites, enhancing CH_4 and CO_2 activation. Specifically, NiCo bimetallic sites drive the formation of key intermediates (e.g., CHO*) from CH_4 and CO_2 activation, avoiding deep CH_4 cracking into C*. This ensures efficient H_2 and CO production while markedly improving catalytic stability through coke inhibition.

Building on our previous research, future development and investigation of photothermally driven catalysts for the dry reforming of methane (DRM) should focus on two key areas. First, precision regulation of strain and defect engineering: exploring heterojunctions with tunable lattice mismatch to quantify the correlation between strain magnitude and catalytic performance, and identifying an "optimal strain window" to maximize C-H activation efficiency. Furthermore, stability can be enhanced through interface modification—via rational synthesis methods and structural design to improve the catalyst’s resistance to sintering and coking. Exploring industrial application directions is equally worthwhile. The ultimate goal of developing DRM catalysts is to enable low-carbon utilization of methane and carbon dioxide; thus, future work should focus on resolving bottlenecks in industrial deployment, such as scalable catalyst synthesis and the development of catalysts

capable of adapting to industrial environments characterized by high temperatures, high pressures, and high levels of impurity gases. These future directions not only underscore the practical value of our current work but also provide clear guidance for subsequent research.

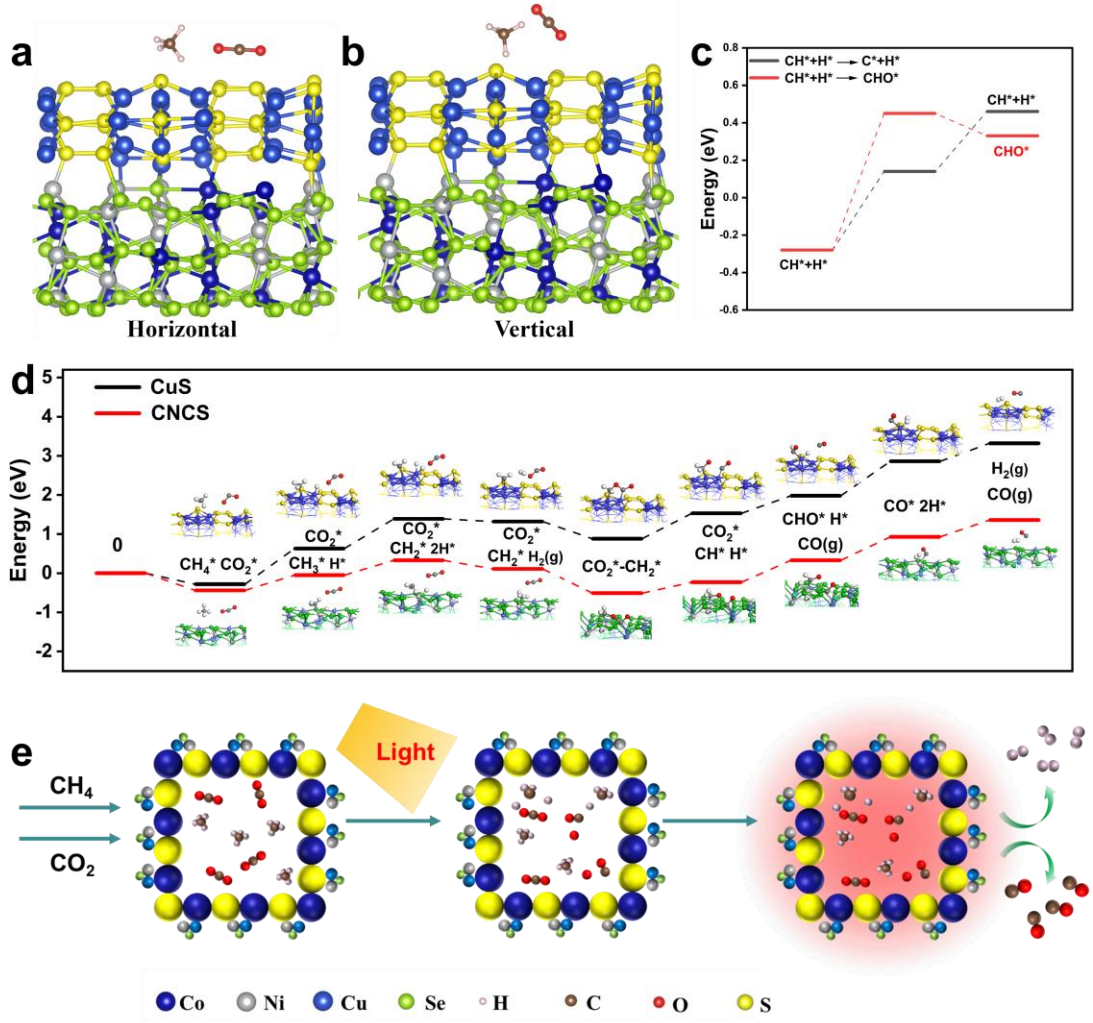

Fig. 5. The structurally optimized adsorption models: (a) horizontal adsorption, (b) vertical adsorption. (c) Transition states of the lowest energy pathways for CHO* path and C*+H* path on CNCS. (d) Reaction energy profiles for DRM path on CNCS. (e) Schematic diagram of photothermal synergistic driven DRM.

4. Conclusion

In summary, this study presents a hollow CuS@NiCoSe heterojunction catalyst that achieves efficient synergy between photothermal conversion and CH_4/CO_2 adsorption-activation during Dry

Reforming of Methane. Unlike previous photothermal catalysts focusing on a single function, this work integrates interface engineering and lattice strain modulation to enhance charge transfer and optimize the electronic structure of active sites. Interfacial lattice strain, induced by strong CuS-NiCoSe bonding, promotes C-H bond cleavage, while the NiCoSe shell ensures broad-spectrum photothermal conversion. Compared with existing studies, the CuS@NiCoSe catalyst exhibits higher catalytic activity (87.7% CH_4 conversion at 650 °C) and superior catalytic stability. This study establishes lattice strain-driven interface engineering as an effective strategy for designing multifunctional photothermal catalysts and provides general design principles for developing advanced multifunctional catalysts for greenhouse gas valorization and sustainable energy conversion.

CRediT authorship contribution statement

Weilong Wang: Conceptualization, Formal analysis, Funding acquisition, Methodology, Project administration, Resources, Supervision, Validation, Writing-review & editing. **Jianfeng Lu:** Visualization, Software, Data curation. **Jing Ding:** Supervision, Project administration, Funding acquisition. **Yukun Hu：** Formal analysis, Methodology. **Zhende Li:** Writing -original draft, Visualization, Validation, Software, Methodology, Formal analysis, Data curation, Conceptualization.

Declaration of Competing Interest

The authors declare that they have no known competing financial interests or personal relationships that could have appeared to influence the work reported in this paper.

Acknowledgements

This paper is supported by National Natural Science Foundation of China (U23A20642). Thanks to eceshi (www.eceshi.com) for XPS and TEM.

Appendix A. Supporting information

Data availability

Data will be made available on request.

References

[1] Pan, F. Xiang, X. Du, Z. Sarnello, E. Li, T. Li, Y. Integrating photocatalysis and thermocatalysis to enable efficient CO_2 reforming of methane on Pt supported CeO_2 with Zn doping and atomic layer deposited MgO overcoating, Applied Catalysis B: Environmental. **2020,** *260,* 118189, https://doi.org/10.1016/j.apcatb.2019.118189

[2] Shen, D.; Li, Z.; Shan, J.; Yu, G.; Wang, X.; Zhang, Y.; Liu, C.; Lyu, S.; Li, J.; Li, L. Synergistic Pt-CeO_2 interface boosting low temperature dry reforming of methane, Applied Catalysis B: Environmental. **2022,** *318,* 121809, https://doi.org/10.1016/j.apcatb.2022.121809

[3] Zhang, Q.; Mao, M.; Li, Y.; Yang, Y.; Huang, H.; Jiang, Z.; Hu, Q.; Wu, S.; Zhao, X. Novel photoactivation promoted light-driven CO_2 reduction by CH_4 on Ni/CeO_2 nanocomposite with high light-to-fuel efficiency and enhanced stability, Applied Catalysis B: Environmental. **2018,** *239,* 555, https://doi.org/10.1016/j.apcatb.2018.08.052

[4] He, C.; Li, Q.; Ye, Z.; Wang, L.; Gong, Y.; Li, S.; Wu, J.; Lu, Z.; Wu, S.; Zhang, J. Regulating Atomically-Precise Pt Sites for Boosting Light-Driven Dry Reforming of Methane, Angew. Chem. Int. Ed. **2024,** *63,* 46, e202412308, 10.1002/anie.202412308

[5] Li, Z.; Lu, J.; Ding, J.; Wang, W. Efficient dry reforming of methane realized by photoinduced acceleration of oxygen migration rate, J. Colloid Interf. Sci. **2024,** *676,* 1001, https://doi.org/10.1016/j.jcis.2024.07.194

[6] Zhang, J.; Xie, K.; Jiang, Y.; Li, M.; Tan, X.; Yang, Y.; Zhao, X.; Wang, L.; Wang, Y.; Wang, X.; Zhu, Y.; Chen, H.; Wu, M.; Sun, H.; Wang, S. Photoinducing Different Mechanisms on a Co-Ni Bimetallic Alloy in Catalytic Dry Reforming of Methane, ACS

Catalysis. **2023,** *13,* 16, 10855, https://doi.org/10.1021/acscatal.3c02525
[7] Palmer, C.; Upham, D. C.; Smart, S.; Gordon, M. J.; Metiu, H.; McFarland, E. W. Dry reforming of methane catalysed by molten metal alloys, Nature Catalysis. **2020,** *3,* 1, 83, https://doi.org/10.1038/s41929-019-0416-2
[8] Ma, M.; Jin, B. J.; Li, P.; Jung, M. S.; Kim, J. I.; Cho, Y.; Kim, S.; Moon, J. H.; Park, J. H. Ultrahigh Electrocatalytic Conversion of Methane at Room Temperature, Advanced Science. **2017,** *4,* 12, https://doi.org/10.1002/advs.201700379
[9] Yao, Y.; Li, B.; Gao, X.; Yang, Y.; Yu, J.; Lei, J.; Li, Q.; Meng, X.; Chen, L.; Xu, D. Highly Efficient Solar-Driven Dry Reforming of Methane on a Rh/LaNiO3 Catalyst through a Light-induced Metal-To-Metal Charge Transfer Process, Adv. Mater. **2023,** *35,* 39, https://doi.org/10.1002/adma.202303654
[10] Sun, J.; Yamaguchi, D.; Tang, L.; Periasamy, S.; Ma, H.; Hart, J. N.; Chiang, K. Advanced Powder Technology. **2022,** *33,* 2, 103407
[11] Haug, L.; Thurner, C.; Bekheet, M. F.; Bischoff, B.; Gurlo, A.; Kunz, M.; Sartory, B.; Penner, S.; Klötzer, B. Zirconium Carbide Mediates Coke-Resistant Methane Dry Reforming on Nickel-Zirconium Catalysts, Angew. Chem. Int. Ed. **2022,** *61,* 50, e202213249, 10.1002/anie.202213249
[12] Wang. L, Wang. R, Wei. S, Li. K, Hasnain Nawaz, He. B, Li. M, Liu. R, Tuning the band gap energy of Cu_xIn_yS for superior photothermocatalytic CO_2 conversion to C_2H_4, Ind. Chem. Mater., **2025**,3, 440-451, https://doi.org/10.1039/D5IM00015G
[13] Peng, H.; Yang, T.; Lin, H.; Xu, Y.; Wang, Z.; Zhang, Q.; Liu, S.; Geng, H.; Gu, L.; Wang, C.; Fan, X.; Chen, W.; Huang, X. Ru/In Dual-Single Atoms Modulated Charge Separation for Significantly Accelerated Photocatalytic H_2 Evolution in Pure Water. Advanced Energy Materials. **2022,** *12,* 43, 2201688, https://doi.org/10.1002/aenm.202201688
[14] Wu, S.; Li, Y.; Zhang, Q.; Hu, Q.; Wu, J.; Zhou, C.; Zhao, X. Formation of NiCo Alloy Nanoparticles on Co Doped Al_2O_3 Leads to High Fuel Production Rate, Large Light-to-Fuel Efficiency, and Excellent Durability for Photothermocatalytic CO_2 Reduction, Advanced Energy Materials. **2020,** *10,* 42, 2002602, https://doi.org/10.1002/aenm.202002602
[15] Sun, C.; Li, Q.; Jia, Z.; Wu, G.; Yin, P. Hierarchically flower-like structure assembled with porous nanosheet-supported MXene for ultrathin electromagnetic wave absorption, Chem. Eng. J. **2023,** *454,* 140277, https://doi.org/10.1016/j.cej.2022.140277
[16] Yang, J.; Wang, J.; Zhao, J.; Bai, Y.; Du, H.; Wang, Q.; Jiang, B.; Li, H. CO2 conversion via dry reforming of methane on a core-shell Ru@SiO2 catalyst, Journal of CO2 Utilization. **2022,** *57,* 101893, https://doi.org/10.1016/j.jcou.2022.101893
[17] Park, J.-H.; Yeo, S.; Chang, T.-S. Effect of supports on the performance of Co-based catalysts in methane dry reforming, Journal of CO2 Utilization. **2018,** *26,* 465, https://doi.org/10.1016/j.jcou.2018.06.002
[18] Tahir, M.; Mansoor, R. Energy & Fuels. **2023,** *37,* 7, 5241
[19] Sun, C. H.; Jia, Z. R.; Xu, S.; Hu, D. Q.; Zhang, C. H.; Wu, G. L. Synergistic regulation of dielectric-magnetic dual-loss and triple heterointerface polarization via magnetic MXene for high-performance electromagnetic wave absorption, J. Mater. Sci. Technol. **2022,** *113,* 128, https://doi.org/10.1016/j.jmst.2021.11.006
[20] Sun, C.; Lan, D.; Jia, Z.; Gao, Z.; Wu, G. Kirkendall Effect-Induced Ternary Heterointerfaces Engineering for High Polarization Loss MOF-LDH-MXene Absorbers,

Small. **2024,** *20,* 48, 2405874, https://doi.org/10.1002/smll.202405874
[21] Zhang, H. Zhang, X. Yang, D. Shuai, Y. Lougou, B. G. Pan, Q. Wang, F. Selection of iron-based oxygen carriers for two-step solar thermochemical splitting of carbon dioxide, Energy Conversion and Management. **2023,** *279,* 116772, https://doi.org/10.1016/j.enconman.2023.116772
[22] Chen, H.-L.; Liu, F.-Y.; Xiao, X.; Hu, J.; Gao, B.; Zou, D.; Chen, C.-C. Visible-light-driven photocatalysis of carbon dioxide and organic pollutants by $MFeO_2$ (M = Li, Na, or K), J. Colloid Interf. Sci. **2021,** *601,* 758, https://doi.org/10.1016/j.jcis.2021.05.156
[23] Zhang, B.-W.; Zhu, M.-N.; Gao, M.-R.; Chen, J.; Xi, X.; Shen, J.; Feng, R.-F.; Semagina, N.; Duan, N.; Zeng, H.; Luo, J.-L. Phase Transition Engineering of Host Perovskite toward Optimal Exsolution-facilitated Catalysts for Carbon Dioxide Electrolysis, Angew. Chem. Int. Ed. **2023,** *62,* 29, e202305552, https://doi.org/10.1002/anie.202305552
[24] Kumar Tailor, N.; Singh, S.; Afroz, M. A.; Pant, K. K.; Satapathi, S. Unraveling the impact of Cu-doping in lead free halide perovskites for markedly enhancing photocatalytic CO_2 reduction performance, Applied Catalysis B: Environmental. **2024,** *340,* 123247, https://doi.org/10.1016/j.apcatb.2023.123247
[25] Jiang, J. Lu, Z. Zhang, M. Duan, J. Zhang, W. Pan, Y. Bai, J, Higher Symmetry Multinuclear Clusters of Metal–Organic Frameworks for Highly Selective CO_2 Capture, J. Am. Chem. Soc. 2018, 140, 51, 17825–17829, https://doi.org/10.1021/jacs.8b07589
[26] Tu, T. N.; Nguyen, P. N.; Kwon, H. T.; Kim, J. Macroporous MOF beads constructed from intergrown MOF nanoparticles for enhancing CO_2 separation, Chem. Eng. J. **2025,** *519,* 164997, https://doi.org/10.1016/j.cej.2025.164997
[27] Wang. Y, Pu. J, An. J, Liang.X, Li.W, Huang. Y, Yang. J, Chen, T, Yao. Y, Tailoring Charge Separationin ZnIn2S4@CdS Hollow Nanocages for Simultaneous Alcohol Oxidationand CO2 Reduction under Visible Light, Inorg, Chem. **2024,** 63, 5269-5280, https://doi.org/10.1021/acs.inorgchem.4c00462
Wang, J.; Zheng, X.; Wang, G.; Cao, Y.; Ding, W.; Zhang, J.; Wu, H.; Ding, J.; Hu, H.; Han, X.; Ma, T.; Deng, Y.; Hu, W. Adv. Mater. **2022,** *34,* 3, 2106354
[28] Rao, Z. Wang, K. Cao, Y. Feng, Y. Huang, Z. Chen, Y. Wei, S. Liu, L. Gong, Z. Cui, Y. Li, L. Tu, X. Ma, D. Zhou, Y. Light-Reinforced Key Intermediate for Anticoking To Boost Highly Durable Methane Dry Reforming over Single Atom Ni Active Sites on CeO2, J. Am. Chem. Soc. **2023,** *145,* 45, 24625, https://doi.org/10.1021/jacs.3c07077
[29] He, C.; Wu, S.; Li, Q.; Li, M.; Li, J.; Wang, L.; Zhang, J. Constructing matched active sites for robust photocatalytic dry reforming of methane, Chem. **2023,** *9,* 11, 3224. https://doi.org/10.1016/j.chempr.2023.06.021
[30] Li, Z. Lu, J.; Ding, J.; Wang, W. Sulfur-induced electronic structure rearrangement at Ru sites for strengthening dry reforming of methane, Chem. Eng. J. **2025,** *508,* 160925, https://doi.org/10.1016/j.cej.2025.160925
[31] Pan, F.; Xiang, X.; Deng, W.; Zhao, H.; Feng, X.; Li, Y. Mechanism of Carbon Monoxide Dissociation on a Cobalt Fischer–Tropsch Catalyst, ChemCatChem. **2018,** *10,* 5, 940, https://doi.org/10.1002/cctc.201701936
[32] Y. Wang, J. Yang, X. Qin, J. Zhuang, W. Yin, T. Chen, Y. Yao, Integrating photogenerated charge carriers for hydrogen production on noble-metal free

dual-photocatalyst under visible light, Composites Part B, **2022**, 241, 110012, https://doi.org/10.1016/j.compositesb.2022.110012
[33] Gavrilova, N. N.; Sapunov, V. N.; Skudin, V. V. Intensification of dry reforming of methane on membrane catalyst, Chem. Eng. J. **2019,** *374,* 983, https://doi.org/10.1016/j.cej.2019.05.168
[34] Henych, J.; Šťastný, M.; Němečková, Z.; Mazanec, K.; Tolasz, J.; Kormunda, M.; Ederer, J.; Janoš, P. Bifunctional TiO2/CeO2 reactive adsorbent/photocatalyst for degradation of bis-p-nitrophenyl phosphate and CWAs, Chem. Eng. J. **2021,** *414,* 128822, https://doi.org/10.1016/j.cej.2021.128822
[35] Guo, D.; Lu, Y.; Ruan, Y.; Zhao, Y.; Zhao, Y.; Wang, S.; Ma, X. Effects of extrinsic defects originating from the interfacial reaction of CeO2-x-nickel silicate on catalytic performance in methane dry reforming, Applied Catalysis B: Environmental. **2020,** *277,* 119278, https://doi.org/10.1016/j.apcatb.2020.119278
[36] He, D.; Wu, S.; Cao, X.; Chen, D.; Zhang, L.; Zhang, Y.; Luo, Y. Dynamic trap of Ni at elevated temperature for yielding high-efficiency methane dry reforming catalyst, Appl. Catal. B Environ. **2024,** *346,* 123728, https://doi.org/10.1016/j.apcatb.2024.123728
[37] Ying, L.; Huang, Z.; Dong, Y.; Lin, F.; Ding, J.; Wang, W.; Lu, J. Hybrid nanoarchitectonics of carbon/titanium carbide integrated hydrogel/melamine foam for highly efficient solar steam and thermoelectric power generation, Desalination. **2023,** *549,* 116328, https://doi.org/10.1016/j.desal.2022.116328
[38] Ying, L. Liang, F. Huang, Z. Ding, J. Wang, W. Liu, S; Lu, J. Self-floating gelatin aerogel integrated urchin-like $MoS_2/Mo_5N_6/C$ with hybrid photothermal enhancement for salt-resistant solar desalination, Chem. Eng. J. **2023,** *474,* 145709, https://doi.org/10.1016/j.cej.2023.145709
[39] Sahu, J. Mishra, B. P. Parida, K. ACS Appl. Energy Mater. **2025,** *8,* 1, 388, https://doi.org/10.1021/acsaem.4c02494
[40] Han, W. Chen, Y. Jiao, Y. Liang, S. Li, W. Tian, G. J. Mater. Chem. A. **2022,** *10,* 34, 17642, https://doi.org/10.1039/D2TA03219H
[41] Y. Tang, Y. Li, W. Bao, W. Yan, J. Zhang, Y. Huang, H. Li, Z. Wang, M. Liu, F. Yu. Enhanced dry reforming of CO2 and CH4 on photothermal catalyst Ru/SrTiO3, Applied Catalysis B: Environmenta. **2023,** *338,* 123054. https://doi.org/10.1016/j.apcatb.2023.123054
[42] M. Mao, Q. Zhang, Y. Yang, Y. Li, H. Huang, Z. Jiang, Q. Hu, X. Zhao, Solar-light-driven CO_2 reduction by methane on Pt nanocrystals partially embedded in mesoporous CeO_2 nanorods with high light-to-fuel efficiency**,** Green Chem. **2018**, *20,* 2857–2869, https://doi.org/10.1039/C8GC01058G
[43] K. Takeda, A. Yamaguchi, Y. Cho, O. Anjaneyulu, T. Fujita, H. Abe, M. Miyauchi, **Metal** Carbide as A Light-Harvesting and Anticoking Catalysis Support for Dry Reforming of Methane, Global Chall. **2020,** *4,* 1900067, https://doi.org/10.1002/gch2.201900067
[44] J. Sun, D. Yamaguchi, L. Tang, S. Periasamy, H. Ma, J.N. Hart, K. Chiang, Enhancement of oxygen exchanging capability by loading a small amount of ruthenium over ceria-zirconia on dry reforming of methane, Adv. Powder Technol. **2022**, *33*, 103407, https://doi.org/10.1016/j.apt.2021.103407
[45] J. Yang, J. Wang, J. Zhao, Y. Ba, H. Du, Q. Wang, B. Jiang, H. Li. CO2 conversion via dry reforming of methane on a core-shell Ru@SiO2 catalyst, J. CO2 Util. **2022,** *57,* 101893,

https://doi.org/10.1016/j.jcou.2022.101893
[46] W. Huang, Z. Gan, M. Mei, L. Ye, J. Shen, J. Xu, X. Xu, X. Wang, Y. Liu, X. Fang, Synergy of oxygen vacancies and Ni0 species to promote the coke-resistance of Ni/Nd2Zr2O7 catalyst for dry reforming of methane. Chem. Eng. J. **2025,** 523, 168481, https://doi.org/10.1016/j.cej.2025.168481
[47] Y. Zhang, N. Cao, K. Wang, M. Yan, X. Zhang, P. Xie, Atomically Dispersed Rh–O–V Pairs Promote Methane Dry Reforming with Sustained Catalytic Activity. ACS Catal. **2025**, 15, 11, 8833–8845, https://doi.org/10.1021/acscatal.5c00625
[48]Z. Gao, M. Cai, J. Zhang, J. Wang, C. Liu, P. Guo, X. Mou, R. Lin, J. Liu, Design of technical Ni@Silicate-1 catalysts for dry reforming of methane. Chem. Eng. J. **2025,** 512, 162223, https://doi.org/10.1016/j.cej.2025.162223